2020 IEEE/RSJ International Conference on Intelligent Robots and Systems (IROS)
October 25-29, 2020, Las Vegas, NV, USA (Virtual)

3D Printed Bio-Inspired Hair Sensor for Directional Airflow Sensing

Keshav Rajasekaran[1], Hyung Dae Bae[2],Sarah Bergbreiter[3], Miao Yu[1]

Abstract— **With reduction in the scale of unmanned air vehicles, there is an increasing need for lightweight, compact, low-power sensors and alternate sensing modalities to facilitate flight control and navigation. This paper presents a novel method to fabricate a micro-scale artificial hair sensor that is capable of directional airflow sensing. The sensor consists of a high-aspect ratio hair structure attached to a thin flexible membrane. When subjected to airflow, the hair deflection induces a deformation of the membrane. Two pairs of perpendicular electrodes are attached to the membrane, which allow the sensing of airflow amplitude and direction through the measurement of differential capacitance. The sensor structure is fabricated by using two photon polymerization, which is integrated onto a miniature PCB circuit board to allow simple measurement. The sensor's responses to static displacement loading from different directions were characterized, and are in good agreement with the simulation results. Finally, the sensor's capability for directional airflow measurement was demonstrated with a clear correlation between flow speed and sensor output.**

I. Introduction

There is a growing interest in developing micro air vehicles (MAVs). MAVs are commonly defined as being smaller than $15\,\mathrm{cm}$ in any dimension [1]. MAVs are smaller, lighter, and more agile than traditional unmanned air vehicles (UAVs). Furthermore, MAVs often have low unit costs and thus can be deployed in larger swarms. Owing to these advantages, MAVs find increasing use in tasks like source localization [2], cooperative surveillance [3], post disaster surveying [4], geological fieldwork [5] and indoor exploration [6] to name a few. Though the small scale of MAVs offer plenty of advantages over UAVs, they are at the same time more susceptible to external disturbances like wind gusts [7]. They also have smaller payloads [8], which makes it difficult to equip them with traditional airflow sensors like anemometers to facilitate flight control. Therefore there is a need for compact, low-power and lightweight flow sensors that can be used be used by MAVs.

Many biological systems solve the issue of flight control under disturbances at this scale through the use of hair-like mechanosensors to measure fluid flow around an locomoting organism. For example, fruit flies have been shown to use their antennae as wind sensors to stabilize their flight in windy environments [9]. Fish utilize mechanosenors along their lateral line to measure flow fields [10]. Bats possess a wide array of sensory hairs that are spread across the wing to provide them with information on flow magnitude and direction [11]. Desert locusts [12], wood crickets [13] and spiders [14] sense flow using mechanosensors on their bodies. Most of these mechanosensors take the form of high aspect ratio hair-like structures. The deflection of these hairs due to flow is detected by sensitive nerve bundles present at their roots [15].

Taking inspiration from biology, researchers have developed various artificial hair flow sensors (AHSs). These vary widely in working principle and transduction mechanism. By far the most common methods involve measuring the flow-induced strain by using either changes in resistance [16]–[23] or capacitance [24]–[27]. Other sensing methods including measuring optical wavelength shift with a fibre Bragg Grating (FBG) [28] or using piezoelectric effect to generate a voltage [29] have also been explored. To create sensors at scales similar to biological hairs, researchers often employ microelectromechanical systems (MEMS) fabrication techniques. These techniques require long processing times and multiple steps in a cleanroom environment. Researches have used non cleanroom processes to fabricate parts of their sensors but have to resort to a clean room environment to achieve sub mm feature sizes necessary for other parts of their senors. Integrating these senors to measurement circuitry or robotic applications can also prove to be complicated.

Two-photon polymerization (2PP) is a direct laser writing technique (DLW) that is growing in popularity [30], [31]. It has been used extensively in fields like microfluidics [32]–[34] and optics [35]–[37], due to its ability to create free-form 3D structures with high feature resolution. Spatial resolutions of $80\,\mathrm{nm}$ have been achieved by researches [38]. Functional robotic mechanisms with a resolution of $3\,\mu\mathrm{m}$ have been realised using 2PP [39]. Leveraging this technique to fabricate AHSs would provide flexibility in geometric design as well as simplfy and reduced processing steps that need a cleanroom. This does, however, trade off the batch processing capabilities of traditional MEMS processes.

In this paper, we report a fully 3D printed micro-scale AHS that was fabricated using 2PP and a subsequent metal deposition step. As the sensor fabrication was based on a one-step printing process, the processing time and complexity were reduced significantly. Integration of the sensor to measurement circuitry was also simplified by embedding parts of the sensor into the printed circuit board (PCB) design. The sensor response to both displacement and airflow were demonstrated experimentally.

[1]K. Rajasekaran and M. Yu are with the Department of Mechanical Engineering, University of Maryland, College Park, MD 20742, USA. Author for correspondence: keshavr@umd.edu

[2]H. D. Bae is with the Department of Mechanical Engineering, Howard University, Washington, DC 20059, USA.

[3]S. Bergbreiter is with the Department of Mechanical Engineering, Carnegie Mellon University, Pittsburgh, PA 15213, USA

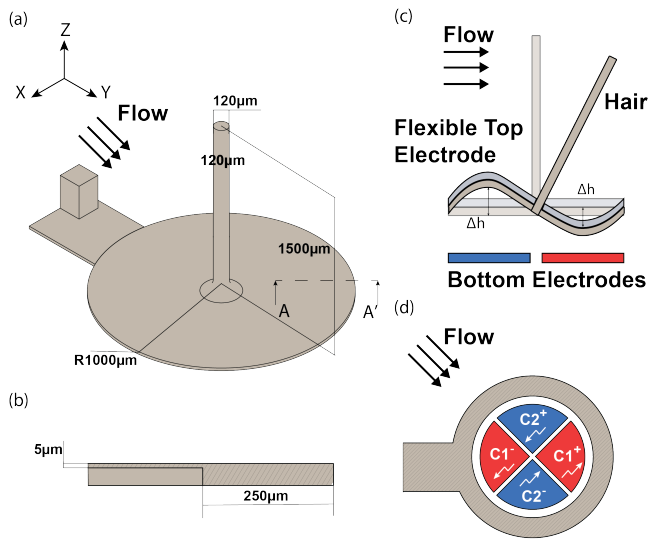

Fig. 1. Design and working principle of 3D printed artificial hair flow sensor (a) Isometric view of sensor with dimension, (b) Zoomed in view of section A-A' with dimensions of the membrane and the supporting ring (c) Schematic showing membrane deflection under airflow, (d) The capacitance change for each electrode under the membrane deflection shown in Fig. 1(c).

II. Sensor Design and Fabrication

A. Working principle

The sensor structure consists a high-aspect ratio pillar (hair), $120\,\mu m$ in diameter and $1500\,\mu m$ in height, placed at the center of a membrane,$5\,\mu m$ in thickness and a $1000\,\mu m$ in radius. A supporting ring $250\,\mu m$ wide and $15\,\mu m$ high holds and suspends the membrane over four bottom electrodes. So the effective electrode gap was $20\,\mu m$. The suspended membrane acts as a flexible top electrode for four capacitors. The four split bottom electrodes are built into the PCB, resulting in two electrode pairs in perpendicular directions. A handle is included in the sensor design to aid in manipulation and assembly during fabrication. Fig. 1(a) is a schematic of the sensor illustrating the important dimensions.

The working principle of the sensor is similar to previously developed artificial flow sensors. The drag due to airflow causes the hair to bend. The bending deforms the flexible membrane that the hair is printed on. This deformation varies the distance between the flexible top electrode and the four bottom electrodes that are present on the PCB. The changes in capacitance caused by this deformation are measured as the sensor output. By obtaining the differential capacitance changes between two pairs of capacitors, both flow magnitude and direction can be determined.

This general operating principle is illustrated in Fig. 1(b-c). When the membrane deflects towards the bottom electrodes, there is an increase in the measured capacitance, $C1^+$,$C2^-$ in the schematic, and when it moves away, the capacitance decreases, $C1^-$,$C2^+$ in the schematic. The differential signal between the two electrode pairs($C1^+ - C1^-$,$C2^+ - C2^-$) is measured as the sensor output. The direction of flow is measured by comparing the capacitance change across the perpendicular electrode pairs.

B. Sensor Fabrication

The sensor was fabricated using two photon polymerization with a Nanoscribe Photonic Professional GT tool (Nanoscribe GmbH, Karlsruhe/Germany). The setup uses a $780\,nm$ pulsed femtosecond laser source. The sensor was designed using Solidworks and the exported STL file was converted to General Writing Language(GWL) by using Nanoscribe's De-Scribe software (v 2.5.4). The GWL files were then loaded into the NanoWrite software (v 1.8.13) for printing. The printing was done by using a 25x/1.4 objective lens (Zeiss) in DiLL mode, where the lens makes direct contact with the resin. The sensor was printed with a scan speed of $50\,000\,\mu m\,s^{-1}$ and a laser power of $75\,mW$.

The complete fabrication process is illustrated in Fig. 2. Initially a layer of Dextran was spin-coated onto a clean ITO slide. The Dextran acts as a sacrificial layer so that the printed sensor can be released from the slide without damaging the membrane. The sacrificial layer was made by mixing Dextran (Sigma-Aldrich) with deionized water in a $1:10$ ratio by weight.

The complete structure was printed in the next step in IPS (a propriety Nanoscribe GmbH photocurable polymer) . After the printing process, the structures were developed by submerging them in propylene glycol monomethyl ether acetate (PGMEA; Sigma-Aldrich) for four hours. This step was intended to remove any uncured polymer that might have been present after the printing process. Channels were designed into the sensor to help remove uncured material from under the floating membrane. The slide was then submerged in IPA for cleaning and dried at room temperature. The sensor was released from the slide by dissolving the dextran layer in deionized water.

A layer of silver, $1000\,Å$ thick was deposited on the floating membrane using E-beam metal deposition. The metal layer functions as the top electrode for the capacitive sensor.

The final step involved assembling the printed structure with the electrodes that were embedded into the PCB that held the necessary measurement electronics. The structure was assembled onto the PCB manually under a microscope using a UV curable polymer (Dymax OP-4-20641) as a fastener. The polymer was then cured by exposing it to UV light ($320\,nm$ to $395\,nm$) for $180\,s$. Conductive silver paste was utilized to connect the top electrode to the PCB. Fig. 3 shows a scanning electron microscope (SEM) image of the completed sensor assembled on the PCB.

III. Sensor Characterization

A. Displacement Loading Tests: Varying Displacement Amplitude

The fabricated sensor was initially tested with a displacement stimulus under a probe station. The experimental results were compared with COMSOL simulations to better understand the sensor performance. A electromechanical forces multiphysics simulation was run with the sensor design. Material properties for IPS reported in [40] were

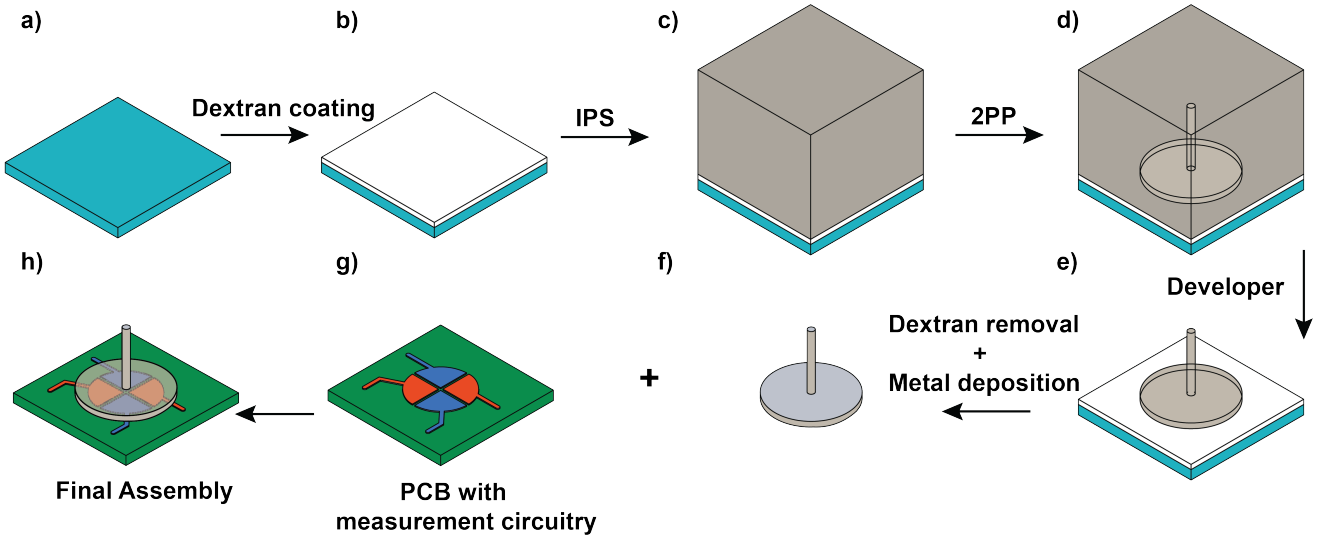

Fig. 2. Fabrication procedure for 3D printed AHS. (a) An indium tin oxide coated glass slide is cleaned using Isopropyl alcohol. (b) Spin coating a 1:10 ratio by weight solution of dextran with deionized water on the slide. (c) Adding a drop of photoresist to the coated slide. (d) The sensor is printed using 2PP. (e) The printed sensor is developed in PGMEA to remove uncured material. (f) Dextran layer is removed and metal is deposited on the membrane using EBeam metal deposition. (g) The sensor is glued to the PCB using a UV polymer. (h) Final fully assembled sensor.

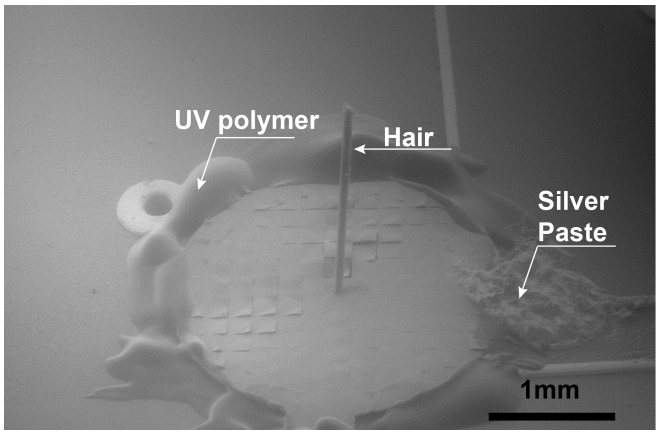

Fig. 3. SEM image of assembled sensor. The sensor is held down using a UV curable polymer and conductive silver paste is used to connect the membrane to the measurement PCB.

used in the simulation. The bottom surface of the bottom electrodes and the bottom surface of the sensor ring were fixed and prevented from displacing. The tip of the hair had a prescribed displacement assigned to it using two global parameters one to control the displacement and another to control the direction. Each of the split bottom electrodes were assigned as a separate terminal with a uniform voltage of 1 V. The top electrode was used as a ground terminal. A parameter sweep over the desired values for both parameters was run and the capacitance change across the terminal were calculated using a global evaluation. The results of the simulation are plotted in Fig. 5(a).

The experimental setup is shown in Fig. 4. The assembled device was mounted on a rotational stage. The probe used to displace the hair was mounted on a 2-axis motorized stage, one to control the horizontal displacement and another to control the height of the probe. Each axis was controlled by a ThorLabs MT1-Z8 motorized stage. The stages were utilized to align the displacement probe with the tip of the hair. The capacitance output from the sensor was obtained by using a capacitance to digital converter (CDC) chip (AD7746, Analog digital). The CDC chip allows for two terminals to be read in a single ended mode or four in a differential mode setup. The differential mode setup was used to obtain the sensor output for all tests. The hair was displaced from 0 µm to 100 µm in 1 µm increments, the probe was held at each position for 5 seconds to ensure the sensor response to reach a steady-state. The assembled sensor was then rotated by 45 degrees in the anticlockwise direction and the test was

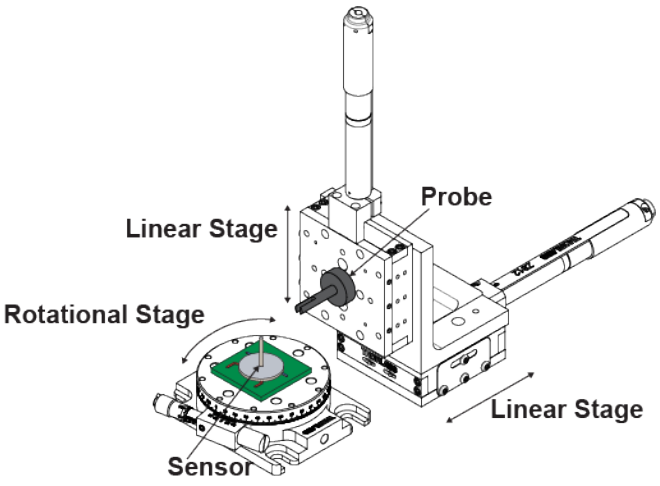

Fig. 4. Schematic of the experimental setup used for performing displacement loading tests. The rotational stage is used to change the direction of stimulus with respect to the bottom electrode pairs. The 2-axis linear stage is used to position the probe with respect to the tip of the hair sensor.

repeated in this new orientation.

The results are shown in Fig. 5(b) with simulation results shown on top and experimental results on bottom. The color-coded lines represent the readouts from the respective electrode pairs. The shaded region surrounding the line in Fig. 5(b)b indicates the standard deviation from a set of 3 trials with the same sensor and the central line indicates the mean.

For the initial orientation (0°) represented by the solid lines, there was no response along the blue electrode pair as the displacement occurred perpendicular to them. In contrast, there was a significant linear decrease in capacitance from the red electrodes as the displacement was applied along this direction. Since the hair was being pushed towards $C1^-$ the capacitance on that electrode increases while the capacitance on $C1^+$ decreases. This causes a net decrease in the differential capacitance readout.

When the sensor was rotated to 45°, the displacement caused equal capacitance decrease across both electrode pairs as expected from the simulation in Fig. 5(a).

Although the sensitivity of the physical sensors are found to be lower than the simulated values, the trend of these results is comparable. The manual assembly step in the fabrication process is believed to affect the sensor performance as seen in the 45° orientation tests. Ideally, the curves for both electrode pairs would overlap perfectly as seen in the simulations Fig. 5(a). Further, the difference in the noise levels for the electrode pairs could also affect the sensor performance. The red electrode pair has a higher noise floor than the blue pair. Other possible contributors to this discrepancy may include electronics placement and improper development during fabrication leaving unexposed resin behind in the printed structure.

B. Displacement Loading Tests: Varying Stimulus Directions

The sensor's ability to distinguish direction of the stimulus was examined by using a constant displacement load with varying directions. The test setup is the same as that used in the previous test. The sensor was rotated from 0° to 90° in 5° increments. At each increment, the tip was deflected by 100 µm and the response was recorded.

The results of the test are shown in Fig. 6. Again these results are color coded to differentiate the corresponding electrode pairs. The diamond markers indicate the sensor response at each angle. The lines are best fit sine curves for the experimental data. The see-saw effect across the best fit curve in the experimental data is due to an artifact of the printing process. Since the sensor was printed layer by layer along the Z axis, the layers on the membrane all aligned along a particular direction. This makes deflection along some angles easier than others, causing the see-saw effect. This can be corrected by rotating alternate layers on the membrane by 90° during the printing process.

C. Air Flow Tests

The sensor's response to airflow was also evaluated experimentally. The setup remains similar to the previous test. The probe was replaced by one end of a polyurethane tube, 5 mm in diameter. The other end of the tube was connected to a pressure controlled compressor. The tube opening was placed 20 mm from the hair sensor. The corresponding velocity at the sensor position was measured by using a portable anemometer and finding the mean flow velocity over a period of 30 s. The flow was directed along the 0° direction. During the experiment, constant flow pressure was applied to the sensor with the help of a control valve until the sensor response stabilized (no more than 5 s. The capacitance change was measured similar to the displacement tests in the previous section.

The results of the flow test are plotted in Fig. 7, which shows the mean capacitance change and standard deviation averaged over 3 trials. The sensor is found to be only capable

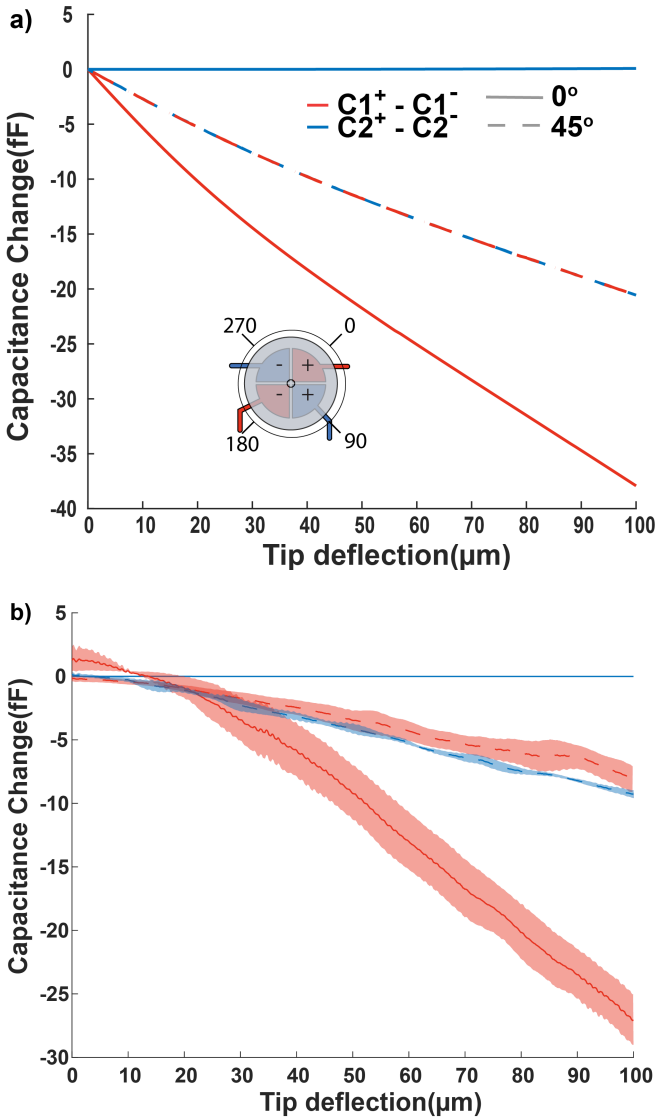

Fig. 5. Sensor pair response to displacement (C1 - blue, C2- red) Bold lines indicate response when displacment is along 0° direction and dashed lines when displacement is along the 45° directions. a) Shows simulation results while b) shows results from experiments. Shaded region around lines indicate standard deviation over 3 trials.

of detecting the flow above $5\,\mathrm{m\,s^{-1}}$.

IV. Discussion

Utilizing The use of microscale 3D printing enables a relatively complex sensor to be manufactured in one simple step followed by metal deposition. Integration with measurement circuitry is simplified by embedding the bottom electrodes into the PCB. The sensor is able to identify both the magnitude and direction of stimulus by measuring capacitance change across two independent and perpendicular axes.

The experimental results demonstrate that the sensor is capable of measuring airflow with speeds between $5\,\mathrm{m\,s^{-1}}$ and $10.2\,\mathrm{m\,s^{-1}}$. Although the experimental results validate the sensor's design and working principle, the flow tests are limited by the use of a compressor to generate flow. The tests need to be repeated in a wind tunnel to better understand the sensor performance in more realistic flow conditions.

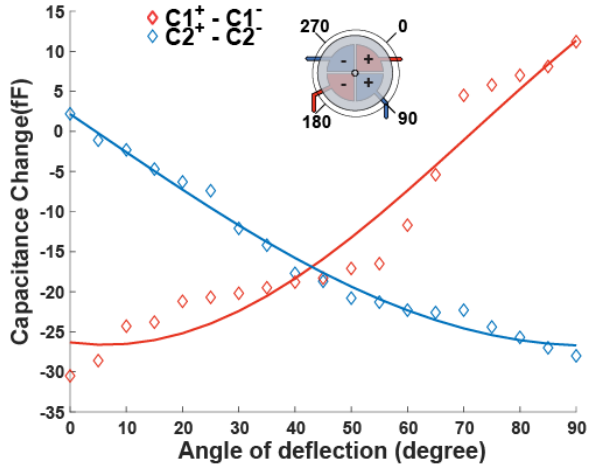

Fig. 6. The sensor pair responses (C1 - blue, C2- red) under different angular deflections. Diamond markers show measured capacitance output while the solid lines are best fit sine functions.

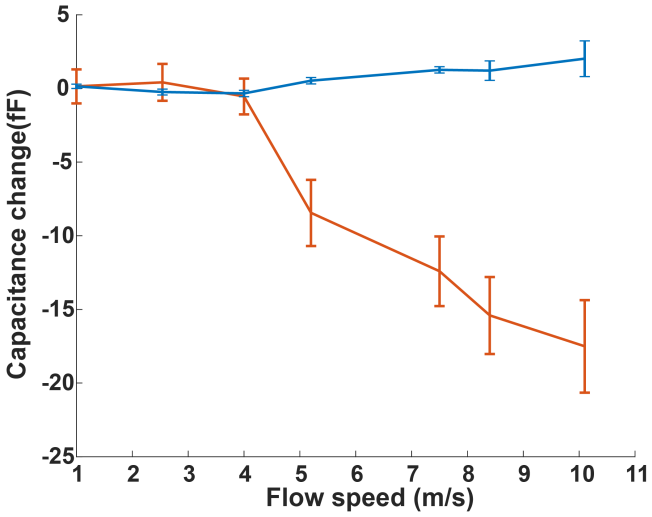

Fig. 7. The sensor pair responses (C1 - blue, C2 - red) under airflow along the 0° direction. Bold lines show mean capacitance output across three trials. Error bars indicate the standard deviation between trials.

We believe that the see-saw effect in the sensor's directional response seen in Fig. 6 is due to the printing process where all the layers on the suspended membrane are aligned in the same direction. Shifting alternate layers by 90° should alleviate this issue. Therefore, addressing the imperfections in the fabrication process can help make the sensor response more symmetric and less noisy. Additionally designing assembly guides onto the PCB and using a better gluing process by cotaing the PCB with a uniform layer of the UV polymer should improve assembly consistency across multiple devices.

Future work would involve studying the sensor in more realistic flow conditions, leveraging the 3D printing process to increases the sensors sensitivity to low flow speeds by adding structural drag enhancers like fins or feathers.

V. Conclusion

This work presents a novel method to fabricate miniature flow sensors. Experimental results validate the sensor's working principle and its ability to discern both the direction and magnitude of a stimulus. The novel fabrication process holds good promise in producing lightweight, compact and sensitive sensors at the same scale as biological hairs, which would greatly benefit the development of future MAVs.

VI. Acknowledgement

This work was supported in part by the Nature-inspired Flight Technologies+Ideas (NIFTI) AFOSR Center of Excellence.

References

[1] T. A. Ward, C. J. Fearday, E. Salami, and N. Binti Soin, "A bibliometric review of progress in micro air vehicle research," *International Journal of Micro Air Vehicles*, vol. 9, no. 2, pp. 146–165, 2017.

[2] M. Saska, J. Langr, and L. Přeučil, "Plume tracking by a self-stabilized group of micro aerial vehicles," in *International Workshop on Modelling and Simulation for Autonomous Systems*. Springer, 2014, pp. 44–55.

[3] M. Saska, J. Chudoba, L. Přeučil, J. Thomas, G. Loianno, A. Třešňák, V. Vonásek, and V. Kumar, "Autonomous deployment of swarms of micro-aerial vehicles in cooperative surveillance," in *2014 International Conference on Unmanned Aircraft Systems (ICUAS)*. IEEE, 2014, pp. 584–595.

[4] V. Baiocchi, D. Dominici, and M. Mormile, "Uav application in post-seismic environment," *International Archives of the Photogrammetry, Remote Sensing and Spatial Information Sciences*, vol. 1, p. W2, 2013.

[5] B. R. Jordan *et al.*, "A bird's-eye view of geology: The use of micro drones/uavs in geologic fieldwork and education," *GSA today*, vol. 25, no. 7, pp. 50–52, 2015.

[6] P. Rudol, M. Wzorek, G. Conte, and P. Doherty, "Micro unmanned aerial vehicle visual servoing for cooperative indoor exploration," in *2008 IEEE Aerospace Conference*. IEEE, 2008, pp. 1–10.

[7] S. Zarovy, M. Costello, A. Mehta, G. Gremillion, D. Miller, B. Ranganathan, J. S. Humbert, and P. Samuel, "Experimental study of gust effects on micro air vehicles," in *AIAA Atmospheric Flight Mechanics Conference*, 2010, p. 7818.

[8] B. N. Ranganathan, I. Penskiy, W. Dean, S. Bergbreiter, and J. S. Humbert, "Bio-inspired wind frame state sensing and estimation for mav applications," in *2015 IEEE/RSJ International Conference on Intelligent Robots and Systems (IROS)*. IEEE, 2015, pp. 2729–2735.

[9] S. B. Fuller, A. D. Straw, M. Y. Peek, R. M. Murray, and M. H. Dickinson, "Flying drosophila stabilize their vision-based velocity controller by sensing wind with their antennae," *Proceedings of the National Academy of Sciences*, vol. 111, no. 13, pp. E1182–E1191, 2014.

[10] H. Bleckmann, "Role of the lateral line in fish behaviour," in *The behaviour of teleost fishes*. Springer, 1986, pp. 177–202.

[11] S. Sterbing-D'Angelo, M. Chadha, C. Chiu, B. Falk, W. Xian, J. Barcelo, J. M. Zook, and C. F. Moss, "Bat wing sensors support flight control," *Proceedings of the National Academy of Sciences*, vol. 108, no. 27, pp. 11 291–11 296, 2011.

[12] J. M. CAMHI, "Locust wind receptors: I. transducer mechanics and sensory response," *Journal of Experimental Biology*, vol. 50, no. 2, pp. 335–348, 1969.

[13] O. Dangles, D. Pierre, C. Magal, F. Vannier, and J. Casas, "Ontogeny of air-motion sensing in cricket," *Journal of Experimental Biology*, vol. 209, no. 21, pp. 4363–4370, 2006.

[14] B. Bathellier, F. G. Barth, J. T. Albert, and J. A. Humphrey, "Viscosity-mediated motion coupling between pairs of trichobothria on the leg of the spider cupiennius salei," *Journal of comparative physiology A*, vol. 191, no. 8, pp. 733–746, 2005.

[15] J. A. Humphrey and F. G. Barth, "Medium flow-sensing hairs: biomechanics and models," *Advances in insect physiology*, vol. 34, pp. 1–80, 2007.

[16] N. Svedin, E. K??lvesten, E. Stemme, and G. Stemme, "A new silicon gas-flow sensor based on lift force," *Journal of Microelectromechanical Systems*, vol. 7, no. 3, pp. 303–308, 1998.

[17] Y. Ozaki, T. Ohyama, T. Yasuda, and I. Shimoyama, "An air flow sensor modeled on wind receptor hairs of insects," *Proceedings IEEE Thirteenth Annual International Conference on Micro Electro Mechanical Systems (Cat. No.00CH36308)*, pp. 531–536, 2000. [Online]. Available: http://ieeexplore.ieee.org/document/838573/

[18] N. Chen, C. Tucker, J. M. Engel, Y. Yang, S. Pandya, and C. Liu, "Design and characterization of artificial haircell sensor for flow sensing with ultrahigh velocity and angular sensitivity," *Journal of Microelectromechanical Systems*, vol. 16, no. 5, pp. 999–1014, 2007.

[19] C. Abels, A. Qualtieri, T. Lober, A. Mariotti, L. D. Chambers, M. De Vittorio, W. M. Megill, and F. Rizzi, "Bidirectional biomimetic flow sensing with antiparallel and curved artificial hair sensors," *Beilstein Journal of Nanotechnology*, vol. 10, pp. 32–46, 2019. [Online]. Available: https://www.beilstein-journals.org/bjnano/articles/10/4

[20] A. G. P. Kottapalli, C. W. Tan, M. Olfatnia, J. M. Miao, G. Barbastathis, and M. Triantafyllou, "A liquid crystal polymer membrane MEMS sensor for flow rate and flow direction sensing applications," *Journal of Micromechanics and Microengineering*, vol. 21, no. 8, 2011.

[21] H. Takahashi, A. Nakai, and I. Shimoyama, "Waterproof airflow sensor for seabird bio-logging using a highly sensitive differential pressure sensor and nano-hole array," *Sensors and Actuators A: Physical*, vol. 281, pp. 243–249, 2018. [Online]. Available: https://www.sciencedirect.com/science/article/pii/S0924424718306460

[22] S. D. Gollob, Y. Manian, R. S. Pierre, A. S. Chen, and S. Bergbreiter, "A lightweight, compliant, contact-resistance-based airflow sensor for quadcopter ground effect sensing," in *2018 IEEE International Conference on Robotics and Automation (ICRA)*. IEEE, 2018, pp. 7826–7831.

[23] H.-S. Shin, T. Kim, S. Bergbreiter, and Y.-L. Park, "Biomimetic soft airflow sensor with printed ionogel conductor," in *2019 2nd IEEE International Conference on Soft Robotics (RoboSoft)*. IEEE, 2019, pp. 611–616.

[24] G. J. M. Krijnen, M. Dijkstra, J. J. van Baar, S. S. Shankar, W. J. Kuipers, R. J. H. de Boer, D. Altpeter, T. S. J. Lammerink, and R. Wiegerink, "MEMS based hair flow-sensors as model systems for acoustic perception studies." *Nanotechnology*, vol. 17, no. 4, pp. S84–S89, 2006.

[25] M. M. Sadeghi, R. L. Peterson, and K. Najafi, "Micro-hydraulic structure for high performance bio-mimetic air flow sensor arrays," pp. 29.4.1–29.4.4, 2011. [Online]. Available: http://ieeexplore.ieee.org/ielx5/6123666/6131464/06131638.pdf?tp={&}arnumber=6131638{&}isnumber=6131464{%}5Cnhttp://ieeexplore.ieee.org/xpls/abs{_}all.jsp?arnumber=6131638{&}tag=1

[26] M. M. Madeghi, R. L. Peterson, and K. Najafi, "A 2-D DIRECTIONAL AIR FLOW SENSOR ARRAY MADE USING STEREOLITHOGRAPHY AND MEMS MICRO-HYDRAULIC STRUCTURES Mahdi M . Sadeghi , Rebecca L . Peterson , and Khalil Najafi Center for Wireless Integrated MicroSensing and Systems (WIMS 2) University of Michigan," *Transducers 2013*, no. June, pp. 722–725, 2013. [Online]. Available: http://stacks.iop.org/0960-1317/23/i=8/a=085017?key=crossref.219e34936bb76f5d6a2f68389e7a70e2

[27] N. Izadi, M. J. De Boer, J. W. Berenschot, and G. J. Krijnen, "Fabrication of superficial neuromast inspired capacitive flow sensors," *Journal of Micromechanics and Microengineering*, vol. 20, no. 8, 2010.

[28] B. J. Wolf, J. A. S. Morton, W. N. MacPherson, and S. M. van Netten, "Bio-inspired all-optical artificial neuromast for 2D flow sensing," *Bioinspiration & Biomimetics*, 2018. [Online]. Available: http://iopscience.iop.org/10.1088/1748-3190/aaa786

[29] M. Asadnia, A. G. P. Kottapalli, K. D. Karavitaki, M. E. Warkiani, J. Miao, D. P. Corey, and M. Triantafyllou, "From Biological Cilia to Artificial Flow Sensors: Biomimetic Soft Polymer Nanosensors with High Sensing Performance," *Scientific Reports*, vol. 6, no. 1, p. 32955, 2016. [Online]. Available: http://www.nature.com/articles/srep32955

[30] S. Maruo, O. Nakamura, and S. Kawata, "Three-dimensional microfabrication with two-photon-absorbed photopolymerization," *Optics letters*, vol. 22, no. 2, pp. 132–134, 1997.

[31] S. Kawata, H.-B. Sun, T. Tanaka, and K. Takada, "Finer features for functional microdevices," *Nature*, vol. 412, no. 6848, pp. 697–698, 2001.

[32] W. Xiong, Y. S. Zhou, X. N. He, Y. Gao, M. Mahjouri-Samani, L. Jiang, T. Baldacchini, and Y. F. Lu, "Simultaneous additive and subtractive three-dimensional nanofabrication using integrated two-photon polymerization and multiphoton ablation," *Light: Science & Applications*, vol. 1, no. 4, pp. e6–e6, 2012.

[33] Y.-J. Liu, P.-Y. Chen, J.-Y. Yang, C. Tsou, Y.-H. Lee, P. Baldeck, and C.-L. Lin, "Three-dimensional passive micromixer fabricated by two-photon polymerization for microfluidic mixing," *Sensors and Materials*, vol. 26, no. 2, pp. 39–44, 2014.

[34] A. C. Lamont, E. C. Reggia, and R. D. Sochol, "In situ nano 3d printing of a microfluidic diode," in *2017 IEEE 30th international conference on micro electro mechanical systems (MEMS)*. IEEE, 2017, pp. 1304–1307.

[35] R. Guo, S. Xiao, X. Zhai, J. Li, A. Xia, and W. Huang, "Micro lens fabrication by means of femtosecond two photon photopolymerization," *Optics express*, vol. 14, no. 2, pp. 810–816, 2006.

[36] J. Kumpfmueller, K. Stadlmann, Z. Li, V. Satzinger, J. Stampfl, and R. Liska, "Two-photon-induced thiol-ene polymerization as a fabrication tool for flexible optical waveguides," *Designed Monomers and Polymers*, vol. 17, no. 4, pp. 390–400, 2014.

[37] N. Kedia, Z. Liu, R. D. Sochol, J. Tam, D. X. Hammer, and A. Agrawal, "3-d printed photoreceptor phantoms for evaluating lateral resolution of adaptive optics imaging systems," *Optics letters*, vol. 44, no. 7, pp. 1825–1828, 2019.

[38] J.-F. Xing, X.-Z. Dong, W.-Q. Chen, X.-M. Duan, N. Takeyasu, T. Tanaka, and S. Kawata, "Improving spatial resolution of two-photon microfabrication by using photoinitiator with high initiating efficiency," *Applied physics letters*, vol. 90, no. 13, p. 131106, 2007.

[39] M. Soreni-Harari, R. St. Pierre, C. McCue, K. Moreno, and S. Bergbreiter, "Multimaterial 3d printing for microrobotic mechanisms," *Soft Robotics*, vol. 7, no. 1, pp. 59–67, 2020.

[40] Y. Liu, O. Stein, J. H. Campbell, L. Jiang, N. Petta, and Y. Lu, "Three-dimensional printing and deformation behavior of low-density target structures by two-photon polymerization," in *Nanoengineering: Fabrication, Properties, Optics, and Devices XIV*, vol. 10354. International Society for Optics and Photonics, 2017, p. 103541U.